

NO-1198 100

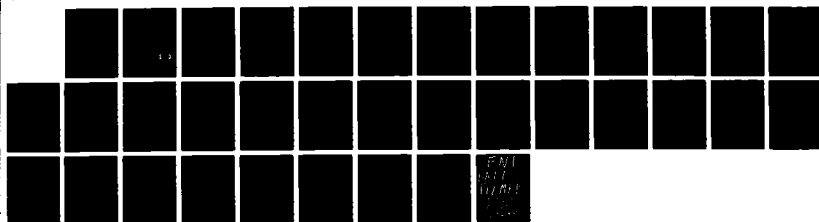
MEASUREMENTS OF THE THERMOSPHERIC MERIDIONAL WIND FROM
THE S05-1 SPACECRAFT (U) AEROSPACE CORP EL SEGUNDO CA
SPACE SCIENCES LAB D C KAYSER 20 JUN 88
TR-0006A(2340-04)-1 SD-TR-88-69

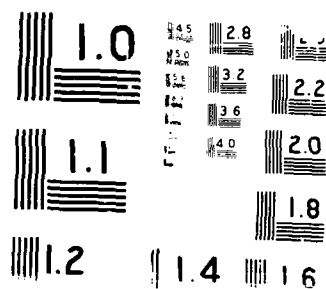
1/1

UNCLASSIFIED

F/G 4/1

NL





DTIC FILE COPY

4

REPORT SD-TR-88-69

Measurements of the Thermospheric Meridional Wind from the S85-1 Spacecraft

AD-A198 100

Prepared by
D. C. KAYSER
Space Sciences Laboratory
Laboratory Operations
The Aerospace Corporation
El Segundo, CA 90245

20 June 1988

Prepared for
SPACE DIVISION
AIR FORCE SYSTEMS COMMAND
Los Angeles Air Force Base
P.O. Box 92960, Worldway Postal Center
Los Angeles, CA 90009-2960

DTIC
ELECTE
AUG 29 1988
S D
CH

APPROVED FOR PUBLIC RELEASE;
DISTRIBUTION UNLIMITED

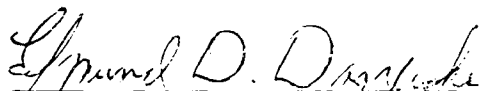
88 8 00 010

This report was submitted by The Aerospace Corporation, El Segundo, CA 90245, under Contract No. F04701-85-C-0086 with the Space Division, P.O. Box 92960, Worldway Postal Center, Los Angeles, CA 90009-2960. It was reviewed and approved for The Aerospace Corporation by H. R. Rugge, Director, Space Sciences Laboratory.

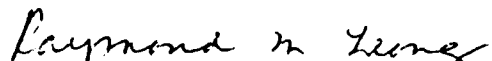
Maj Edmund D. Daszewski was the project officer for the Mission-Oriented Investigation and Experimentation (MOIE) Program.

This report has been reviewed by the Public Affairs Office (PAS) and is releasable to the National Technical Information Service (NTIS). At NTIS, it will be available to the general public, including foreign nationals.

This technical report has been reviewed and is approved for publication. Publication of this report does not constitute Air Force approval of the report's findings or conclusions. It is published only for the exchange and stimulation of ideas.



EDMUND D. DASZEWSKI, Maj, USAF
MOIE Project Officer
SD/WE



RAYMOND M. LEONG, Maj, USAF
Deputy Director, AFSTC West Coast Office
AFSTC/WCO OL-AB

UNCLASSIFIED

SECURITY CLASSIFICATION OF THIS PAGE

REPORT DOCUMENTATION PAGE

1a. REPORT SECURITY CLASSIFICATION Unclassified			1b. RESTRICTIVE MARKINGS		
2a. SECURITY CLASSIFICATION AUTHORITY			3. DISTRIBUTION / AVAILABILITY OF REPORT Approved for public release; distribution unlimited.		
2b. DECLASSIFICATION / DOWNGRADING SCHEDULE					
4. PERFORMING ORGANIZATION REPORT NUMBER(S) TR-0086A(2940-04)-1			5. MONITORING ORGANIZATION REPORT NUMBER(S) SD-TR-88-69		
6a. NAME OF PERFORMING ORGANIZATION The Aerospace Corporation Laboratory Operations		6b. OFFICE SYMBOL (If applicable)	7a. NAME OF MONITORING ORGANIZATION Space Division		
6c. ADDRESS (City, State, and ZIP Code) El Segundo, CA 90245			7b. ADDRESS (City, State, and ZIP Code) Los Angeles Air Force Base Los Angeles, CA 90009-2960		
8a. NAME OF FUNDING / SPONSORING ORGANIZATION		8b. OFFICE SYMBOL (If applicable)	9. PROCUREMENT INSTRUMENT IDENTIFICATION NUMBER F04701-85-C-0086-P00016		
8c. ADDRESS (City, State, and ZIP Code)			10. SOURCE OF FUNDING NUMBERS		
			PROGRAM ELEMENT NO	PROJECT NO	TASK NO
			WORK UNIT ACCESSION NO		
11. TITLE (Include Security Classification) Measurements of the Thermospheric Meridional Wind from the S85-1 Spacecraft					
12. PERSONAL AUTHOR(S) Kayser, D. C.					
13a. TYPE OF REPORT		13b. TIME COVERED FROM _____ TO _____		14. DATE OF REPORT (Year, Month, Day) 1988, June 20	
				15. PAGE COUNT 35	
16. SUPPLEMENTARY NOTATION					
17. COSATI CODES			18. SUBJECT TERMS (Continue on reverse if necessary and identify by block number)		
FIELD	GROUP	SUB-GROUP	Spectrometer Wind measurements		
19. ABSTRACT (Continue on reverse if necessary and identify by block number)					
<p>The Upper Atmosphere Composition Spectrometer (UACS) was flown on the Department of Defense Space Test Program mission S85-1. UACS was designed to measure neutral composition, temperature, and the in-track wind component in the lower thermosphere. In the high inclination orbit of S85-1, UACS measured the meridional component of wind at all but the highest latitudes. While techniques to measure cross-track neutral wind have been successfully demonstrated by other investigators, in situ measurements of the in-track wind component have not been published before. UACS obtained a small but significant set of wind data for two days in July 1984 at altitudes between 200 and 235 km, at local solar times of 10.5 and 22.5 hours. The measured winds compare favorably with published results from ground-based incoherent-scatter radar and Fabry-Perot interferometer experiments as well as with satellite-based cross-track measurements of the meridional wind.</p>					
20. DISTRIBUTION / AVAILABILITY OF ABSTRACT <input checked="" type="checkbox"/> UNCLASSIFIED//LIMITED <input type="checkbox"/> SAME AS RPT <input type="checkbox"/> DTIC USERS			21. ABSTRACT SECURITY CLASSIFICATION Unclassified		
22a. NAME OF RESPONSIBLE INDIVIDUAL			22b. TELEPHONE (Include Area Code)		22c. OFFICE SYMBOL

DD FORM 1473, 84 MAR

83 APR edition may be used until exhausted
All other editions are obsolete

SECURITY CLASSIFICATION OF THIS PAGE

UNCLASSIFIED

CONTENTS

I. INTRODUCTION.....	5
II. INSTRUMENTATION.....	7
III. TECHNIQUE AND DATA ANALYSIS.....	11
IV. A COMPARISON WITH OTHER MEASUREMENTS OF THE MERIDIONAL WIND COMPONENT.....	21
V. DISCUSSION.....	29
REFERENCES.....	31

Approved For		<input checked="" type="checkbox"/>
M. J. HALL		
Date		
Signature		
Date		
by		
Distribution		
Availability		
Dist		
A-1		

FIGURES

1.	A Schematic of the UACS Sensor.....	8
2.	Detail of the Ion Source Ionization Region.....	9
3.	Normalized Detector Signal (Data) for N_2 vs Retarding Potential Voltage.....	14
4.	UACS Uncorrected Wind Measurements in the Satellite Reference Frame	16
5.	Combined Data Sets of the Summer Nighttime Meridional Wind.....	17
6.	Combined Data Sets of the Summer Daytime Meridional Wind.....	18
7.	Magnetic (24-hr A_p) and Solar Flux (S_a) Conditions Were Quiet for the Measurement Period ^a in July 1984.....	20

TABLES

1.	Ground-Based Measurements of the Meridional Wind.....	22
2.	Ground Station Coordinates.....	25
3.	Meridional Wind Data from Atmosphere Explorer-E.....	25

I. INTRODUCTION

There are a number of relatively new satellite-based techniques used to measure various components of the thermospheric neutral wind field. A Fabry-Perot interferometer (FPI) (Ref. 1) was flown on Dynamics Explorer-B (DE-B) (Ref. 2) for remote sensing of the meridional wind component. This instrument measured the Doppler shift of the thermospheric $O(^1D)$ line to derive winds for altitudes between 150 and 350 km (Ref. 3). Subject to the availability of appropriate emission features, this technique is accurate (30 m s^{-1}) and is presumably adaptable to cross-track wind measurements. The satellite electrostatic triaxial accelerometer (SETA) has also been used to measure cross-track (horizontal) winds in situ (Ref. 4). This technique is applicable in the altitude region of significant satellite drag, usually below 230 km, and its accuracy is dependent on the mass and cross section of the vehicle and on such factors as satellite noise and vibration. A random error of 60 m s^{-1} at 170 km was quoted in the above work.

Techniques for wind measurement employing neutral-mass spectrometers have also been demonstrated. A system which used a single moving baffle to modulate the incoming gas stream was flown by Spencer et al. (Ref. 5) on Atmosphere Explorers (AE) -C, -D, and -E. The vertical cross-track wind component was measured on AE-C (Ref. 6) while the horizontal cross-track (meridional) wind component was measured on AE-E with 50 m s^{-1} or better accuracy at 260 km altitude (Ref. 7). Exploiting spin modulation of the fly-through mode signal, Knutson et al. (Ref. 8) used the Open-Source Neutral-Mass Spectrometer (Refs. 9, 10) on AE-D to measure the vertical wind component at auroral latitudes. In order to measure both cross-track components of the neutral wind, a dual baffle system was employed by the wind and temperature spectrometer (WATS) (Ref. 11) which was flown on DE-B.

To date, there are no published reports of a successful in situ measurement of the in-track component of neutral wind. In principle, this wind component could be obtained from an energy analysis of the incident gas stream. Philbrick et al. (Ref. 12) obtained a retarding potential curve for neutrals with a velocity mass spectrometer. Hanson and Heelis (Ref. 13) described a variety of techniques for measurement of ion and neutral winds, including the one for neutral retarding potential analysis (RPA). Since then,

there have been attempts to make this measurement on AE-E (Ref. 13), Pioneer Venus Orbiter (Ref. 14), and DE-B (Ref. 11). Sensing of the in-track wind component is required to measure meridional wind at all latitudes from a polar-orbiting satellite. Combined with the WATS dual baffle technique, this additional capability would enable a complete specification of the neutral wind as was done on DE-B with WATS and FPI (Ref. 3). However, measurements of all wind components by mass spectrometer would be obtained entirely in situ and would be independent of atmospheric emission features.

The upper atmosphere composition spectrometer (UACS) was flown on Department of Defense Space Test Program mission S85-1 in the summer of 1984. The orbit was nearly polar at ~ 84 degree inclination with equatorial crossings at approximately 10.5 and 22.5 hours local solar time. UACS measurements were obtained at various times from July 19 through August 7, while perigee and apogee were 202 and 253 km, respectively.

In an earlier paper, Kayser et al. (Ref. 15) described the UACS in some detail and included preliminary examples of normal and fly-through mass spectra. Also shown was an RPA sweep on the molecular nitrogen peak. Since then, an analysis of the RPA mode and its operation has been completed. The wind data obtained from this mode have been reduced and compared with previous wind measurements from other sources. Although the UACS RPA data set is small, it is sufficient to demonstrate successful application of the technique to neutral wind measurements.

II. INSTRUMENTATION

Details on the operation of UACS were covered in an earlier paper (Ref. 15). A brief description is included herein. Figure 1 is a cross-sectional view of the sensor with its vacuum cover removed. A portion of the cover mechanism (A) remains but is out of view of the sensor due to collimator B. The incident gas enters the collimator from the left and impinges on the ion source chamber (C). Two redundant electron guns (D), which are normal to the sensor axis (and to each other), produce a 50- μ A electron beam which is used to ionize the gas. The ions are extracted (normal mode) or drift (in RPA and fly-through modes) into the lens (E) which accelerates and focuses the beam into the electric quadrupole filter (F). Ions of the selected mass exit the quadrupole where 96% are collected in the electrometer cup (G). The remaining 4% exit through the back of the cup and are deflected by the electrostatic deflector H into the spiraltron electron multiplier (I). At the beginning of each 0.1 second sample period, a decision is made by the electrometer monitor circuit whether to activate the deflector. In this way, a large dynamic range can be achieved while protecting the multiplier from excessive count rates. The RPA signal is proportional to the ambient, rather than source, gas density and therefore is inherently small. At the given high altitude of operation, all RPA signals were measured on the multiplier.

Figure 2 shows the ionizing chamber in greater detail. The parts shown are all cylindrically symmetric about the neutral beam direction. As in Fig. 1, neutrals enter from the left, are ionized by the crossed electron beam, and are extracted into the lens on the right. The 75 eV electron beam is collected on the circular collector ring which is part of the filament control circuit. For RPA work, shells 1 and 2 are driven equally at a voltage which brings the average exit energy (and quadrupole drift energy) of the selected species to 10 eV. Hence, for N_2 which impinges with 8.9 eV energy, this voltage is 1.1 V. For atomic oxygen the voltage increment is 4.7 V. With the mass filter tuned to a selected mass, the retarding grid is driven in steps of 0.25 V between \approx 6 and 16 V, bracketing the expected energy distribution.

The sensor output signal is proportional to the number of ions with energies exceeding the barrier energy. A typical signal from the RPA analysis at 233 km is shown in Fig. 3. Forty-one voltage steps are executed at a rate

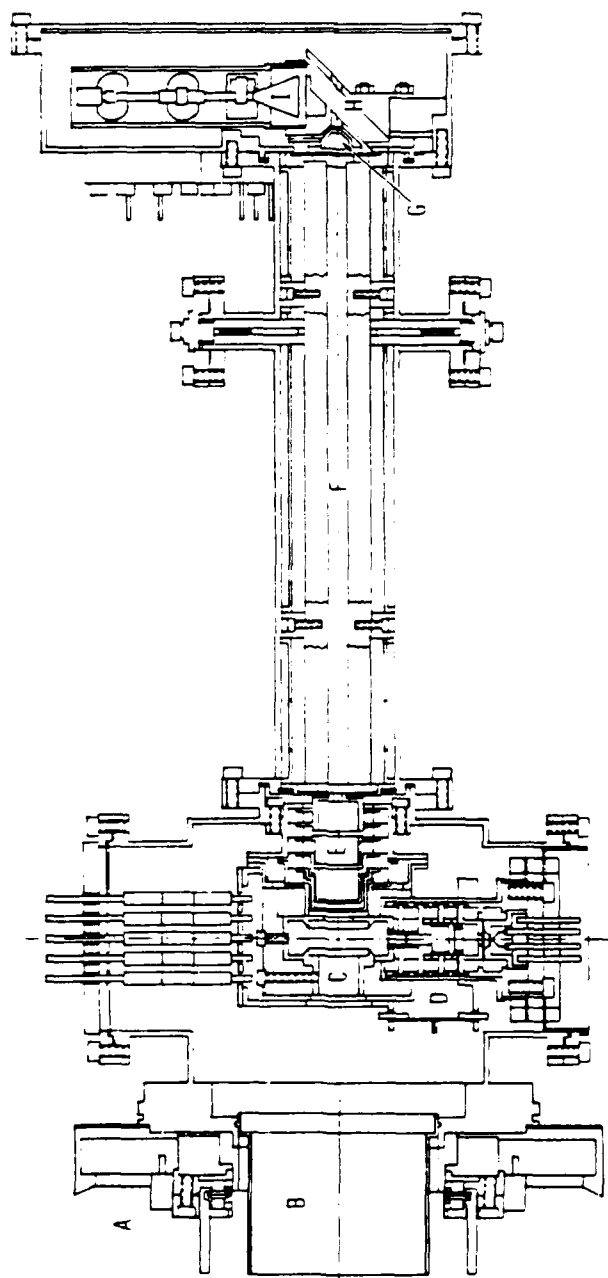


Fig. 1. A Schematic of the UACS Sensor. The ambient gas stream enters from the left through collimator B. Ion source region is C, D, and E. F is the electric quadrupole mass filter. Components of the dual detector are found at G, H, and I.

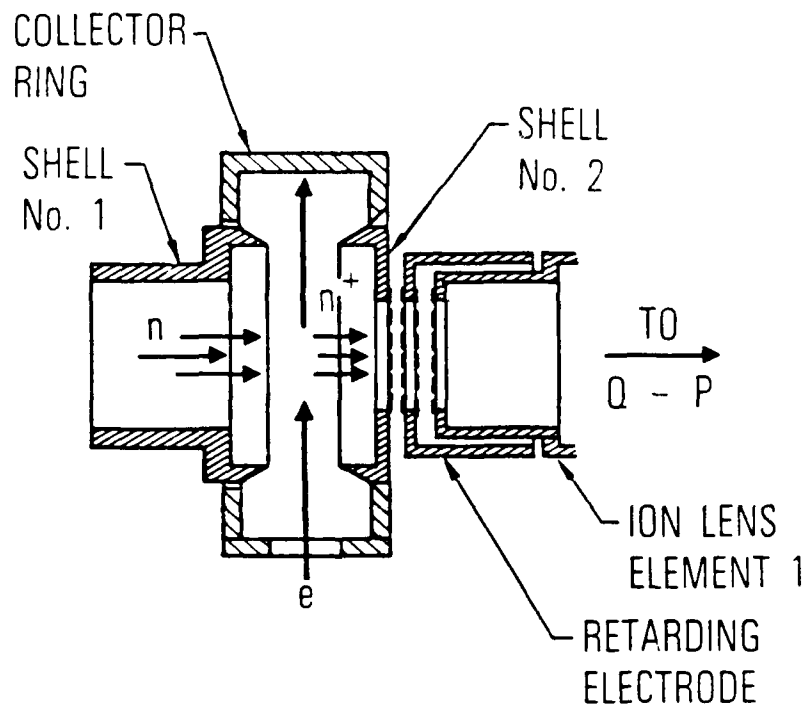


Fig. 2. Detail of the Ion Source Ionization Region. Neutrals enter from the left, are ionized by the crossed electron beam and extracted to the right. Shells 1 and 2 define a drift region in the RPA mode and an extraction region in normal mode. The retarding grid is held at ground for normal mode but is driven by a ramp generator to perform the RPA.

of ten steps per second. Not shown are normal-mode points taken before and after the sweep and between voltage steps 20 and 21. Also not shown are points in the tail above 14 V, that are not significant for the analysis, and a number of "housekeeping" steps that are executed at the beginning of the timing cycle. With extraneous steps included, a total of 5 seconds (39 km distance along the track) are used in one energy measurement.

III. TECHNIQUE AND DATA ANALYSIS

In an ideal system, the RPA response curve would be proportional to an integral of the incident gas energy distribution function, $f(E)$, where the integral is taken over all energies $E=eV$ ($V>V_r$) and where V_r is the instantaneous retarding voltage. Absolute particle energies would be obtained directly from the calibrated RPA sweep voltage. In practice, a number of instrumental characteristics modify the overall transmission factor. These characteristics include the response of the mass filter, any field leakage from the ion lens through the retarding grid, off-axis ion discrimination, residual electric fields in the source drift region, and any electron beam potential. In consequence, the RPA curve is proportional to an integral over $q(V, V_r, \dots) f(eV)$, where q is a function of instrument-related variables. Due to the factors represented by q , the inherent absolute calibration is lost and some laboratory calibration is necessary.

A typical UACS RPA curve is shown in Fig. 3. Provided that q is a slowly varying function of V over the energy range of 6 to 16 eV, the main effect of small wind-related shifts in the energy of the incident gas is to change the position (and to a lesser degree, the shape and amplitude) of the RPA curve. In this circumstance, changes in position should be a direct measure of wind over the expected (<1000 m/s) range. The kinetic energy represented by the 50% amplitude point is $eV_R - E_0 - dE$ which is, to a first approximation, equivalent to the velocity expression $1/2 m(v_s + w)^2$, where V_R is the retarding voltage at the 50% amplitude point on the RPA curve, E_0 is any energy increment imparted to the ion by the source field configuration (e-beam or drift space related), dE is a gas pressure correction to E_0 , m is the ion mass, and v_s is the satellite velocity. Solving for the in-track wind w gives

$$w = [2(eV_R - E_0 - dE)/m]^{1/2} - v_s. \quad (1)$$

As a final step, w must be corrected for any component of the rotating atmosphere parallel to the satellite velocity vector.

Preferably, the RPA mode would be calibrated in a neutral beam facility to establish an exact relationship between the RPA voltage scale and the neutral beam velocity. Lacking this, a rough laboratory calibration was

established as follows: The instrument was operated with a static sample gas and with source voltage settings which would produce nominal 10 eV ions at the retarding grid. Then the normal mode voltage differential between shells 1 and 2 was reduced in steps and at each step the RPA curve was measured. From these data, energy shifts in the curve due to combined electron beam and source potentials could be calculated. The energy shift inferred for zero potential difference between shells was taken as E_0 . To this laboratory value, a correction was added to account for adjustments of source voltages made during preflight calibration. E_0 was determined to be $+0.9 (\pm 0.2)$ eV. Thus, due to the particular combination of source and beam potentials in the present design, the position of the RPA curve was shifted by 0.9 eV toward higher energies. The net increment is positive in spite of the negative well effect of the electron beam because the space between shells 1 and 2 allows the positive collector ring voltage to protrude into the drift space along the axis. For the same reason, when shells 1 and 2 are driven to equal voltages, there remains a nonuniformity in the field of the drift space, which appears as an energy dispersion in the exiting ion beam.

In flight, for the purpose of measuring shifts in the retarding curve (hence wind), it would suffice to fit some empirical function to the sweep data. It is more instructive, however, to approximate the shape of the curve from the ambient gas distribution function and estimates of the instrumental response function q . The laboratory-measured mass-filter response to changes in ion energy was approximated by a capacitor charging curve whose amplitude rises to 63% at 4 eV and to essentially 100% at 10 eV. Placement of dual high-transmission grids shown in Fig. 2 effectively eliminates leakage of the ion lens field through the retarding grid structure. Thus, transmission of ions was set equal to unity for particle energies exceeding eV_r , and to zero otherwise. Off-axis ion transmission was set equal to unity for any ion passing through the aperture of ion lens element, and to zero otherwise. It is likely that the effective radius is actually smaller than the aperture radius, due to the low transmission factor for ions entering the mass filter at large angles. However, using this radius as the approximate extent of the effective ion-producing volume in the electron beam, and employing the calculated source electrostatic field, an energy dispersion can be estimated for the ions. As derived above, the average potential in the production volume is the shell voltage plus E_0 .

With these estimates for q , a trial RPA curve can be calculated for the incident gas energy distribution function. A family of such curves representing different V_R is generated and compared to the RPA sweep data. The curve with the best fit by least-squares criteria yields the best estimate of V_R . Such a result is illustrated in Fig. 3, where the best-fit curve and curves displaced by ± 0.1 V are shown. Even though some of the approximations used in the generation of the curve are crude, the resulting shape is a satisfactory reproduction of the data. With V_R known, Eq. 1 is employed to find w . The least-squares process also yields an error estimate for w . For the wind measurements to be presented, these errors are typically 0.036 eV (15.3 m s^{-1}) at 201 km altitude and 0.049 eV (20.9 m s^{-1}) at 226 km.

While in principle any of the peaks, N^+ , O^+ , N_2^+ , or O_2^+ could be used for the RPA technique, all of the S85-1 wind measurements presented here were derived from retarding potential analysis of the major singly-ionized molecular nitrogen peak at mass 28, thus avoiding possible complications due to contamination by dissociative ionization. Potential contamination of the signal by ambient ions is minimized by the overall ion-optical design of the sensor and by the electric field configuration upstream of the ionization chamber.

In Fig. 4, the derived in-track wind for all local times has been plotted versus latitude using the satellite reference frame. A wind of positive magnitude is a head wind. In this figure only, wind was calculated with $dE=0$. Three separate data segments are shown. Data represented by (-) are all part of a southbound 10.5 LST pass. High northern latitude data (+) are from a second southbound pass. Points (+) between -30 and +12 degrees are from a north-bound pass at 22.5 LST. Due to the higher altitude of the north-bound pass, the signal was weaker and the data scatter larger than for the lower altitude measurements.

A statistical analysis of the data in Fig. 4 indicates that the errors deduced from the above least-squares process should be multiplied by a factor of approximately 1.32 to achieve consistency with overall along-the-track scatter. If this factor is attributed entirely to technique, then typical measurement errors of 20 and 28 m s^{-1} are calculated for the low- and high-altitude passes respectively. Because of the finite angular sensitivity of the sensor and the sharply peaked entrance angle of the neutral beam, a

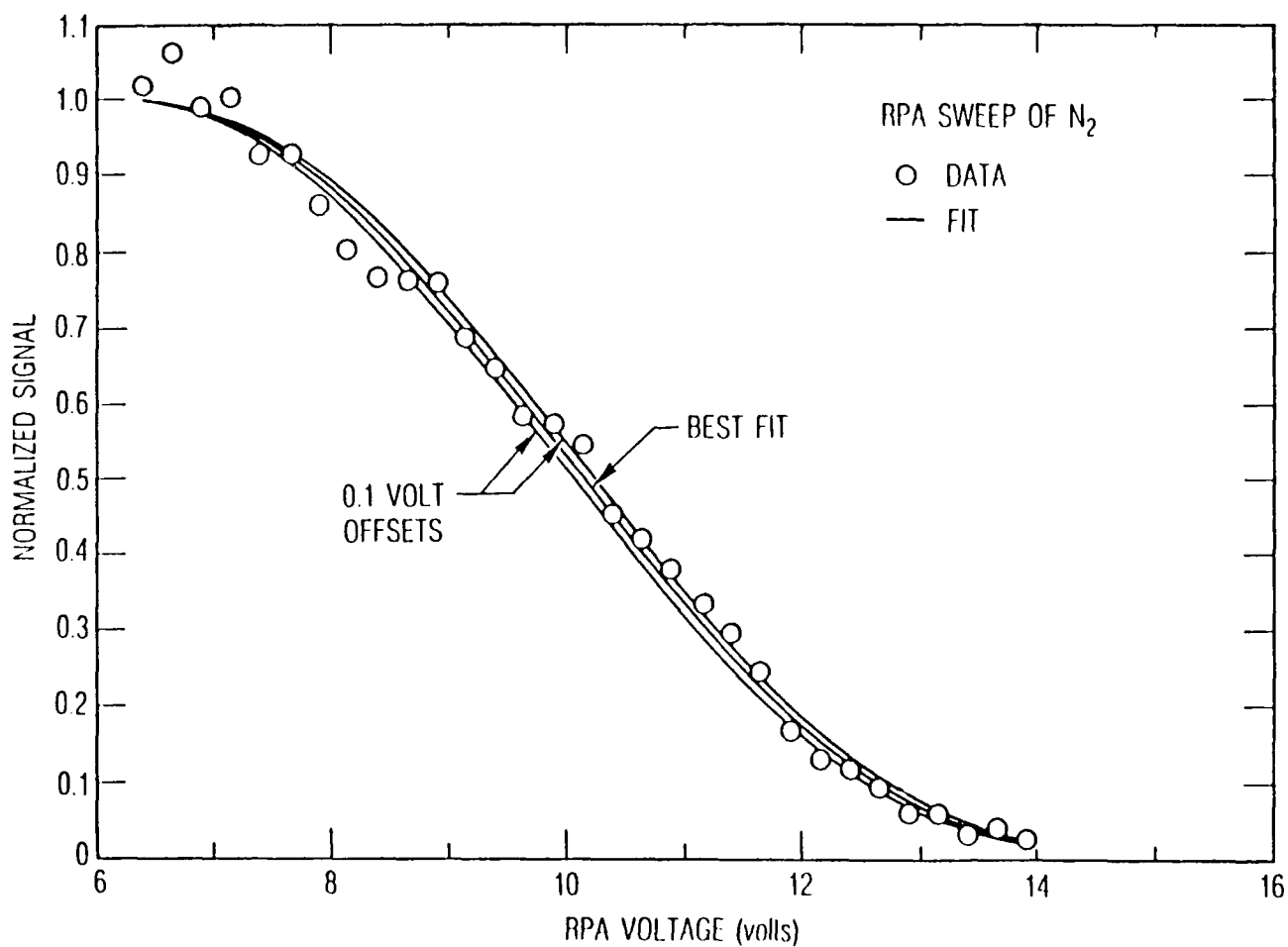


Fig. 3. Normalized Detector Signal (Data) for N_2 vs Retarding Potential Voltage. A best fit curve is shown along with two curves which are displaced 0.1 V either side of the best fit voltage. The curves are the neutral gas distribution function convoluted with the instrument response function.

constant cross wind will change the amplitude of the RPA curve. As a consequence, variations in the cross wind on the time scale of a second could modulate the instantaneous RPA signal, introducing a noise component. This seemingly random variation would contribute to the measurement error. It is likely, therefore, that the factor of 1.32 represents some combination of technique-related errors such as cross-track wind modulation and actual short-term variation in the in-track wind component.

To the extent that laboratory data can be used to fix the quantities in Eq. 1, the measurement technique has no free parameters. Any change in the absolute calibration of the RPA energy scale will be seen in Fig. 4 as a uniform vertical displacement of all points. A 0.1 V change in calibration would shift the pattern by 43 m s^{-1} . It will be demonstrated in succeeding sections that changes much larger than this would lead to systematic disagreements with existing data. Calibration is also influenced by one other parameter, namely the pressure-related energy increment, dE , induced by the electron beam.

Linder and Hernquist (Ref. 16) give an expression for the relationship between neutral gas pressure and the depth of the potential well in an electron beam. Their expression can be used to derive a simplified estimate for changes in potential with pressure, giving

$$dE \approx E_w \ln(p_2/p_1) \quad (2)$$

where E_w is the kinetic energy of the escaping ions at the walls of the chamber and p_2 and p_1 are the final and initial pressures, respectively. A value of 0.112 eV was chosen for E_w . This is four times the energy of thermal ions at 300 K but is consistent with the potential well depth inferred from lab data. p_1 corresponds to the pressure in laboratory measurements wherein the value for E_0 was inferred. It also corresponds to low altitude near the 30-degree latitude point in Fig. 4. Thus, the greatest changes from the dE correction are in the higher altitude 22.5 LST data, shifting this segment by $\sim 60 \text{ m s}^{-1}$ toward zero. In Figs. 5 and 6, these corrected data have been plotted (-) after averaging in two-degree bins. In this form, the data represent the meridional wind component except at latitudes above 55 degrees, where the satellite path introduces a small and unknown zonal component in the in-track wind velocity.

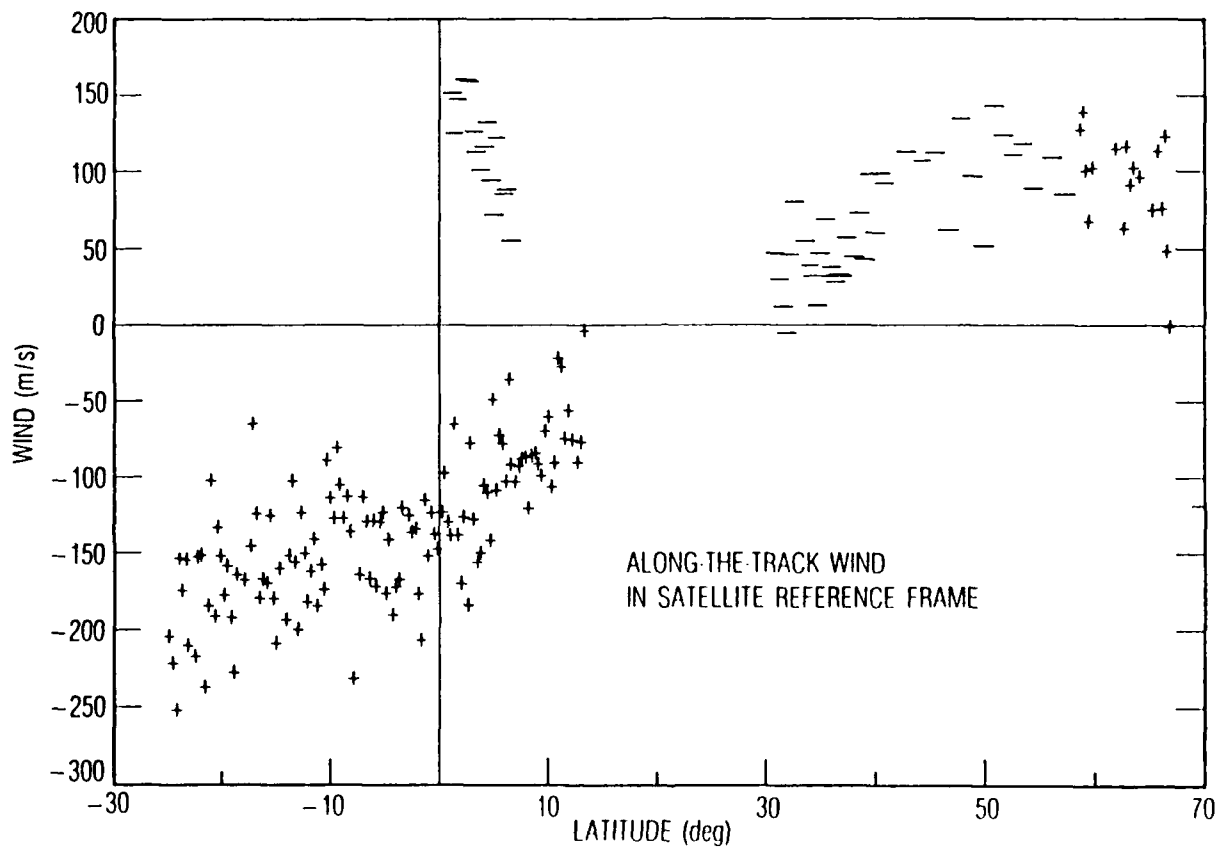


Fig. 4. UACS Uncorrected Wind Measurements in the Satellite Reference Frame. Winds at high northern latitudes and winds with positive values near the equator were measured on southbound passes at 10.5 LST and 205(+5) km. Winds at low latitudes plotted with + symbols were measured on a northbound pass at 22.5 LST and 228(+7) km. In the satellite frame positive wind is a headwind.

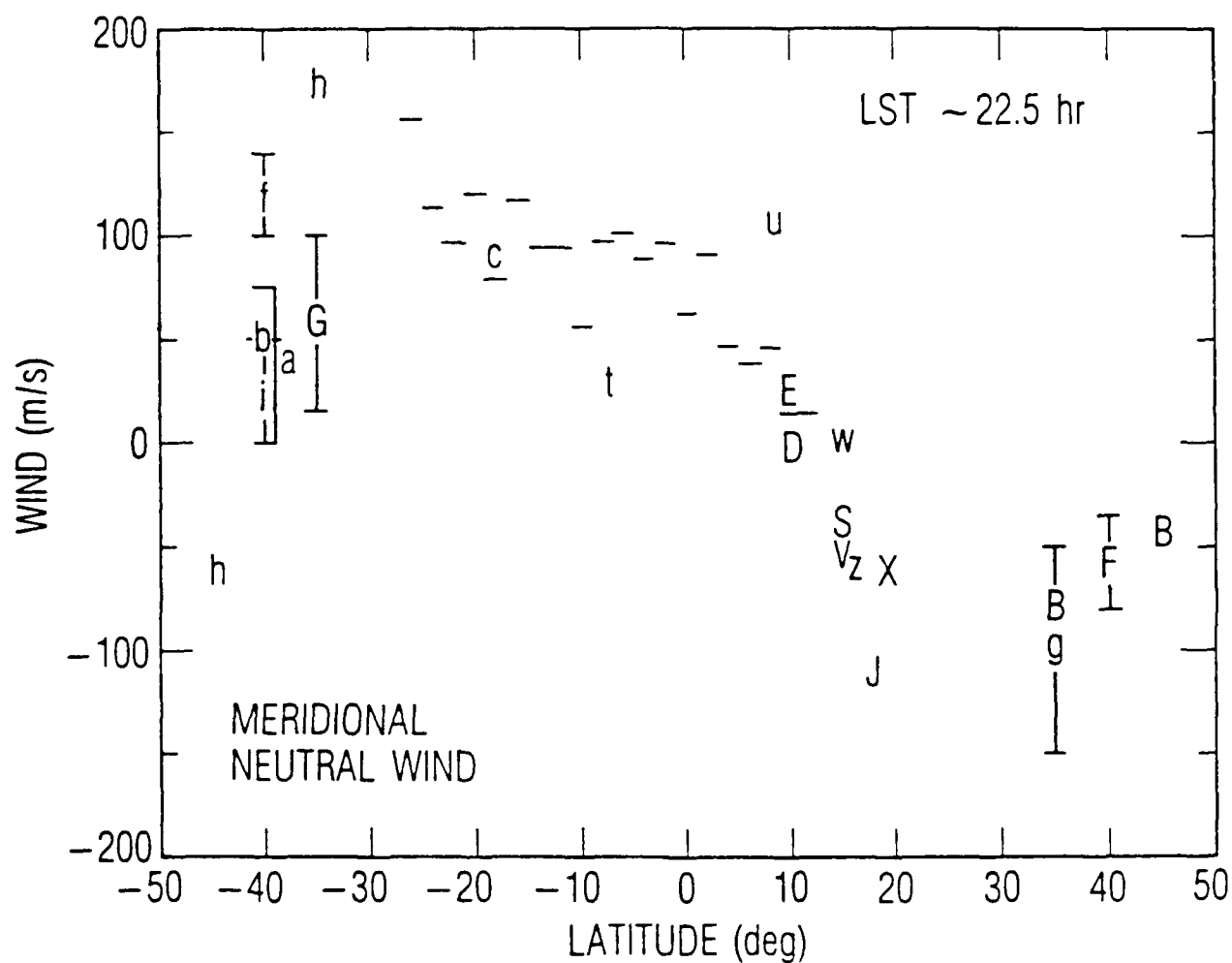


Fig. 5. Combined Data Sets of the Summer Nighttime Meridional Wind. Dashes are the corrected and smoothed UACS measurements. Letters and letters with vertical bars are previously published data from AE-E and a variety of ground stations. As much as possible, the data shown are associated with solar minimum condition. Winds to the north are positive.

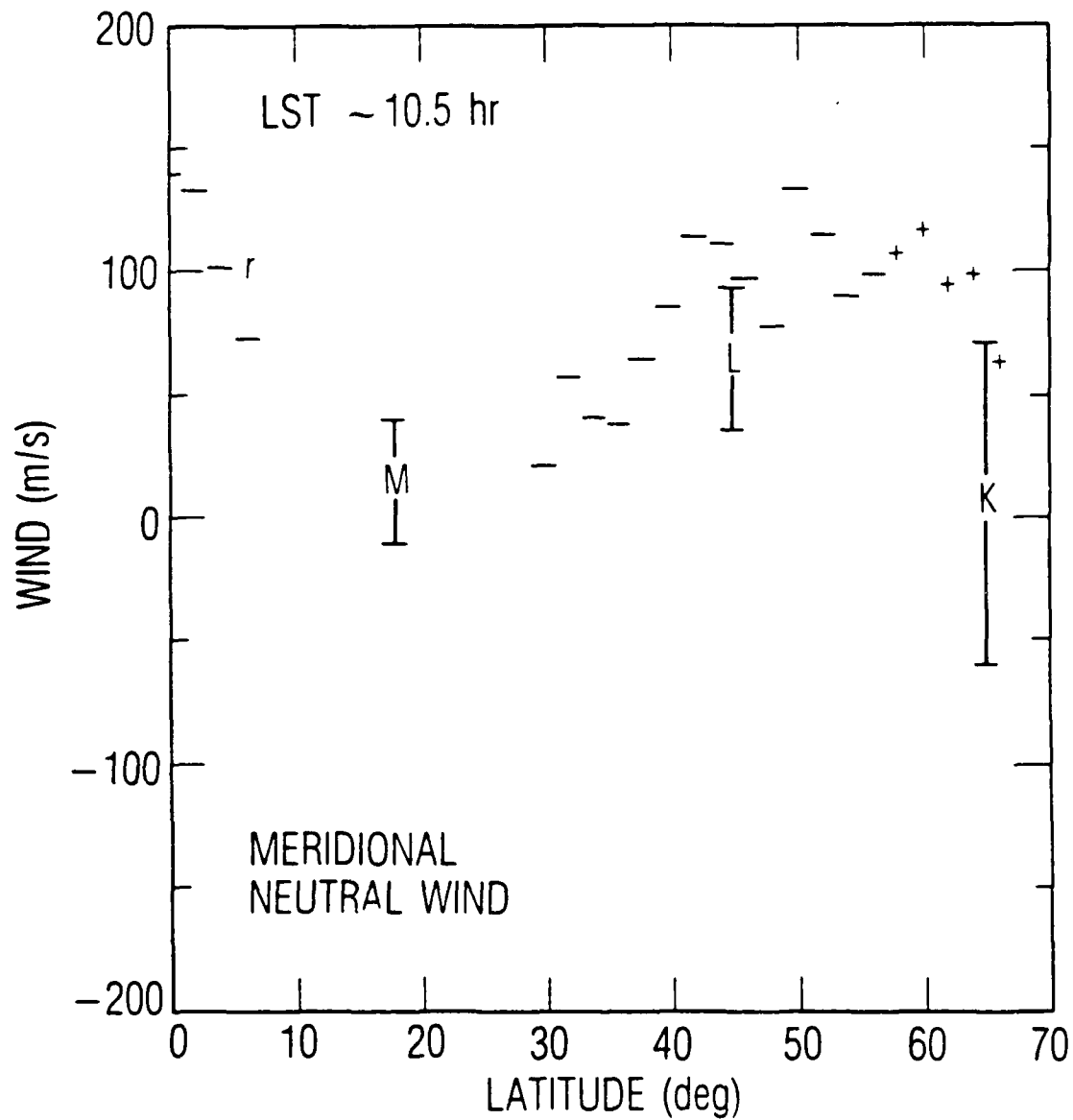


Fig. 6. Combined Data Sets of the Summer Daytime Meridional Wind. Dashes are the corrected and smoothed UACS measurements. Letters and letters with vertical bars are previously published data from AE-E and a variety of ground stations. As much as possible, the data shown are associated with solar minimum condition. Winds to the north are positive.

The measured data should be most typical of solar minimum and geomagnetically quiet times. Figure 7 shows both the solar flux at 1 AU (S_a) and daily magnetic index (A_p) for the latter part of July 1984. On the two days when winds were measured (vertical arrows), the solar flux remained near 85 and the magnetic index was below 20. This circumstance facilitated a comparison with quiet-time data obtained from other sources. In the next section details of the comparison are discussed.

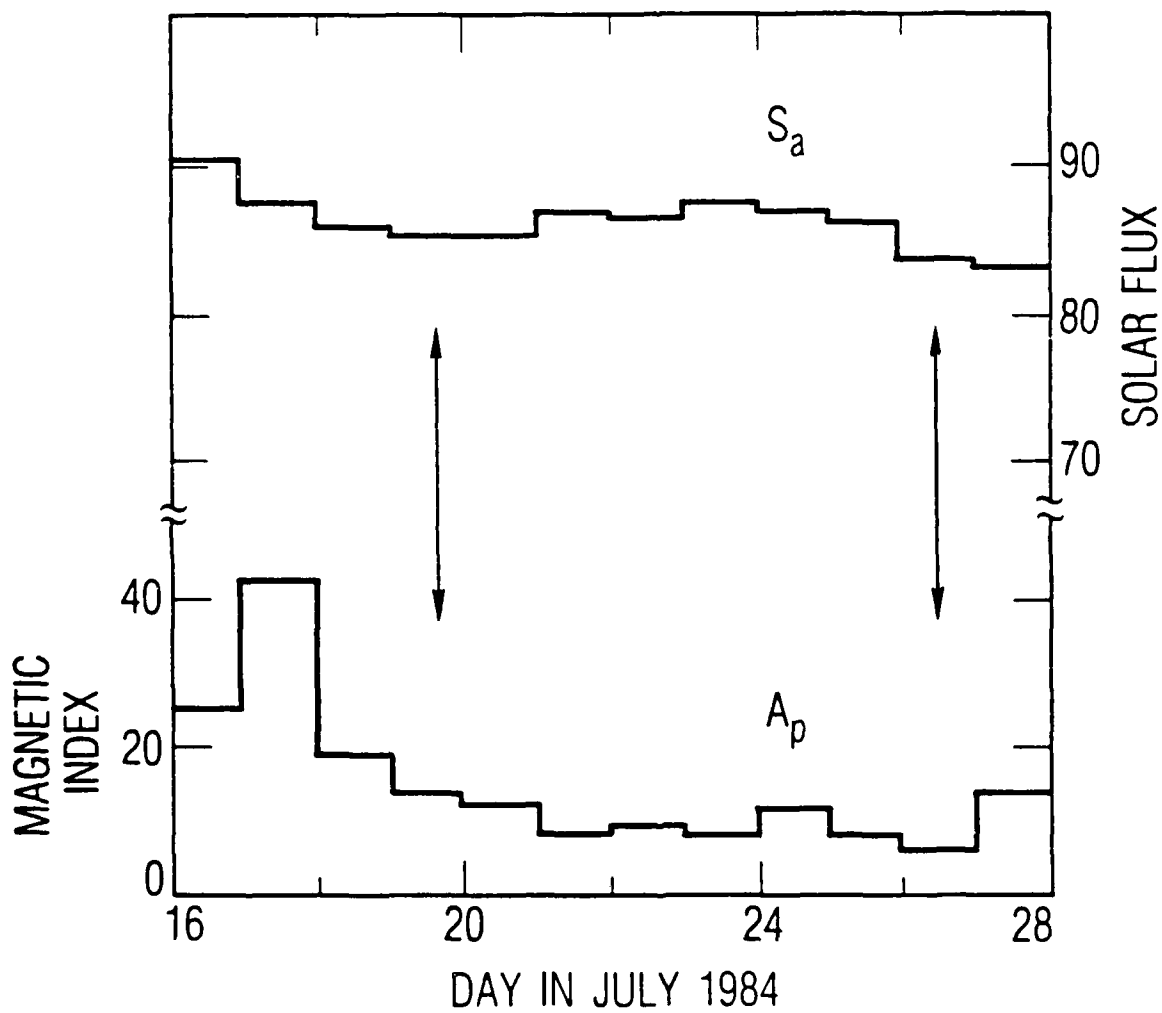


Fig. 7. Magnetic (24-hr A_p) and Solar Flux (S_a) Conditions Were Quiet for the Measurement Period in July 1984. Arrows indicate measurement days.

IV. A COMPARISON WITH OTHER MEASUREMENTS OF THE MERIDIONAL WIND COMPONENT

The present results can be compared with published meridional wind measurements which were derived from incoherent-scatter radar and Fabry-Perot interferometer techniques. Fabry-Perot measurements are available only for nighttime hours, but at a variety of latitudes, whereas radar data are available for both day and night, but with limited latitude coverage. Because UACS data were obtained in a period of low solar and magnetic activity, the comparison excludes much recent ground-based data taken during the present solar cycle. Table 1 summarizes the selected ground-based data set for local times of 10.5 and 22.5 hours that should most closely approximate conditions during the flight of S85-1. These data are plotted along with the S85-1 data in Figs. 5 and 6.

The table lists for each data value, the experiment year and day, local solar time, solar flux at 10.7 cm, daily magnetic index A_p , measurement altitude in km, method, a one letter index, and source reference. Some measurements were originally reported as monthly or seasonal averages. In other cases, a range of wind values was inferred by this author to be typical of conditions reported in the original reference. Thus, the day column includes designations such as Wr, Sr, and Eq for Summer, Winter, and Equinox, as well as sequences of single-letter abbreviations for months (M-J-J is May-June-July, for instance). Single data values may represent single measurements or averages. A pair of numbers in parentheses represents a range of velocities. Positive values indicate a northward wind.

The literature includes numerous examples of enhanced meridional wind near midnight [see, for example, Amayenc (Ref. 17) and Burnside (Ref. 18)], with much of the increase after 20-21 hours. Care was taken in the preparation of Table 1 to choose nighttime values as close to 22.5 hours as possible. In some cases it was necessary to make interpolations or small extrapolations from later hours. In two cases values at midnight are listed. As much as possible, measurements at low solar flux and low solar activity were used. Ideally, wind velocities should be corrected to the S85-1 satellite altitude, but there is no reliable way to do this. In the example of Burnside et al. (Ref. 30), even monotonicity with altitude may not be a good assumption.

Table 1. Ground-Based Measurements of the Meridional Wind

Experiment Year	Day	LST (hr)	F10.7	Ap	Altitude (km)	Method	ID	Wind (m/s)	Reference
73-75	Wr	22.5	low	low	250	F-P	a	(-75,0)	(Ref. 19)
73-77	Sr	22.5	low	all	~250	F-P	b	-40	(Ref. 20)
	Sr							-70	
	Wr			low				-50	
86	Jan 14-17	22.5	75	4.5	300	radar	c	-90	(Ref. 18)
77	Aug 21	22.5	90.8	5	~250	F-P	d	0	(Ref. 21)
	20	22.5	88.7	8	~250	F-P	e	20	(Ref. 22)
76-77	Sr	22.5	low	low	250	F-P	f	(-80, -35)	(Ref. 23)
76	Wr	22.5	low	low	250	F-P	f	(-140, -100)	(Ref. 23)
72-73	M-J-J	22.0	med	low	250	F-P	g	15	(Ref. 24)
	A-S-O							90	
	M-J-J	0.0						100	
	A-S-O							100	
	N-D	22.0						(50, 150)	
76	Jan 2	0.0	73.6	4	250	F-P	h	60	(Ref. 25)
		22.5						-175	
75	Nov	22.5	low	low	250	F-P	i	(-50, 0)	(Ref. 26)
	Dec							20	
85	May	22.5	low	low	300	radar	j	-125	(Ref. 27)
71-78	Sr	11.0	all	all	all	radar	k	-60	(Ref. 28)
	Eq							0	
	Wr							70	

Table 1. Ground-Based Measurements of the Meridional Wind (Continued)

Experiment Year	Day	LST (hr)	F10.7	Ap	Altitude (km)	Method	ID	Wind (m/s)
71	July	11.0			300	radar	1	(Ref. 17)
	6		122.8	9				35
	7		118.5	3				62
	8		112.9	8				42
	9		104.2	6				93
74	Aug	11.0			200	radar	m	(Ref. 29)
	10		86	16				40
	12		97	5				40
	13		93	6				-10

The data of Table 1 are plotted in Figs. 5 (22.5 LST) and 6 (10.5 LST) using the single letter identifiers. Capital letters represent data plotted at the measurement location, whereas lowercase letters represent data plotted in the hemisphere opposite from the measurement. Thus, "b" of Fig. 5 was measured in Northern hemisphere winter and has been plotted here as a Southern hemisphere winter value with a sign change in wind direction. Table 2 lists ground station latitudes and longitudes along with the single letter identifiers. In the example of "b", the source was Fritz Peak. Other measurements at this location in summer were reported for low sky elevation angles, giving winds at 35 and 45 degrees latitude. Where a range of values is reported, the letter identifier is found centered in a vertical bracket. No attempt has been made to assign error bars to the referenced measurements.

Table 3 is extracted from meridional wind data published by Spencer et al. (Ref. 7) and Wharton et al. (Ref. 31). These wind measurements were all made in 1977 from the Atmosphere Explorer-E (AE-E) satellite before the onset of the present solar cycle. The orbit of AE-E was nearly equatorial with an inclination of ~19 degrees and altitude between 255 and 280 km. The data of Table 3 are treated in a manner similar to the data of Table 1 which, for these particular data samples, gives the concentration of points plotted in Fig. 5 near the latitude of Arecibo.

Referring to Fig. 5, the S85-1 nighttime measurements between latitudes -37 and +12 degrees are in good agreement with the meridional wind profile implied by the ground-based data (points c, d, e, and h) and are bounded by the AE-E points t and w. The comparison of S85-1 data for 10.5 LST with other measurements (Fig. 6) is also reasonable, but tentative, considering the small number of other points available.

As was mentioned earlier, a zonal wind component may be present in the UACS data at latitudes above 55 degrees N. latitude, placing those values at the high (winter) end of the range measured at Chatanika. On the other hand, as explained by Wickwar et al. (Ref. 28), the lower end of the range was determined by a very few summer observations. We cannot be certain how representative these points might be. The most curious wind values obtained by UACS are those indicating northward flow at 10.5 LST between the equator and 8 degrees N. latitude. While this flow direction does not agree with a simple model of flow away from the solar bulge, there is a supporting data point (r)

Table 2. Ground Station Coordinates

Ground Station	Latitude (deg)	Longitude (deg)	Data
Arecibo	18 N	67 W	c, j, m
Chatanika	65 N	147 W	k
Fritz Peak Obs.	40 N	106 W	a, b ⁺ , h ⁺ , i, b
Kwajelein Atoll	9 N	168 E	d, e
Laurel Ridge	40 N	79 W	f
St.-Santin	45 N	20 E	l
Adelaide	35 S	190 E	g

*Data reported at 35 and 45 deg N.

Table 3. Meridional Wind Data from Atmosphere Explorer-E

Day (1977)	Lat. (deg)	LST (hr)	F _{10.7}	A _p	Wind (m/s)	ID	Reference
Jan. 19	-6	10.5	76.9	8	-100	r	(Ref. 31)
May 21	15	22.5	81.4	4	-40	s	"
Jan 19	7	22.5	76.9	8	-30	t	"
Feb 8	-7	"	78.6	18	-110	u	"
Aug 9	15	"	85.9	20	-50	v	"
Feb 10	-16	"	83.5	12	0	w	(Ref. 7)
Aug 11	19	"	87.6	28	-60	x	"
Nov 15	-16	"	97.9	25	50	z	(Ref. 31)

from Wharton et al. (Ref. 31). Also, in Fig. 6 the range of values measured at Arecibo (M) would appear to agree with reasonable extrapolations of the S85-1 data, both from the south and north. Overall, the above comparisons of UACS wind measurements with other available data provide a high degree of confidence that the RPA technique was working properly.

Beyond the confirmation of an instrumental technique, the meridional wind profiles of Figs. 5 and 6 provide an interesting glance at thermospheric dynamics for typical solar minimum conditions at ~ 250 km and 22.5 LST. In Fig. 5 the overall profile begins at southern winter mid-latitudes, with northerly flow toward the equator. This flow diminishes and reverses in the vicinity of 10 degrees N. At the latitude of Arecibo, the flow is moderate to strong but in the equatorward direction, as has been regularly observed (Ref. 32). The equatorward flow continues at higher latitudes, but with diminishing velocity above 40 degrees N. A few data points for 25-30 degrees N would be very useful. In their absence it is still reasonable to infer that in summer, at this local time and low solar flux, the equatorward flow velocity maximizes around 25 degrees N and is typically 100 m s^{-1} .

The summer flow picture agrees well with a number of general observations. Burnside et al. (Ref. 32) note that in summer the equatorward meridional wind is stronger to the north. Their estimate for the wind gradient of $50\text{-}100 \text{ m s}^{-1}$ per 1000 km agrees well with a value of $60\text{-}80 \text{ m s}^{-1}$ inferred from Fig. 5. Also, in their estimate, the meridional wind goes to zero 500 km to the south, in good agreement with the crossover point implied by the figure. Some caution is necessary in these comparisons because the wind gradients may vary with solar activity and the data of the last reference were obtained at much higher values of $F_{10.7}$.

The winter hemisphere wind profile may be more controversial. Burnside et al. (Ref. 30) report quiescent or even poleward flow for 22.5 LST at Arecibo in winter, with the $F_{10.7}$ solar flux near 200. On the other hand, point C in Fig. 5 is derived from Burnside et al. (Ref. 18) when the solar flux was 75. This point is not inconsistent with the UACS data and the Adelaide data (point G). The winter profile therefore may be typical of solar minimum only or may represent one extreme of wind variability.

A final point of interest is the comparison of Arecibo data (Ref. 27) with winds from AE-E (Refs. 7, 31). In Fig. 5, a number of AE-E points fall

within the Arecibo latitudes, some after a reflection in latitude and season. There is a high degree of consistency among these data and reasonable agreement with the ground-based result (J), allowing for day-to-day variability. Not only is this a good cross-calibration between techniques, but it offers some justification for the use of hemispherically "transplanted" data, at least at low latitudes.

V. DISCUSSION

Overall consistency of the UACS wind measurements with previously published data was demonstrated in the last section. In a sense, it was fortunate that these measurements were done in a higher than anticipated orbit because the bulk of comparison data had been obtained at these altitudes. On the other hand, because of the higher altitude of S85-1, there are several aspects of the measurement technique that were not fully demonstrated but which are important for lower altitude flights.

Only 4% of the available count rate was used to produce the RPA signal. As a consequence, the random error of a single 4-second wind measurement was on the order of 15 to 21 m s^{-1} . Had the instrument been designed specifically for wind measurements in a narrow altitude range, a factor of up to 25 increase in signal would have been available. While the implied factor of 5 decrease in measurement random error might not be realized, it is probably reasonable to anticipate relative errors of 10-15 m s^{-1} for a repeat experiment which is better matched to the altitude range. Given a more intense signal, another possibility is to sample at a higher rate to achieve increased along-the-track resolution.

Thus, with minor changes in the UACS design, it is expected that in-track wind at 50 km altitude circular could be measured to 20 m s^{-1} (relative error) every 16 km. At lower altitudes, signal strength improves with the scale height of N_2 . Absolute calibration of the instrument for wind to 43 m s^{-1} (0.1 Volt for N_2) or better now appears feasible. Given a large database of such measurements, it may also be possible to define a posteriori, the zero of the RPA, from characteristics of the observed wind field. In general, the measurement technique presented here should be competitive with existing ground- and satellite-based techniques.

When the same technique is used on lower-flying satellites, charge neutralization in the ionizing electron beam may produce an altitude-dependent offset (dE) in the measured ion energy and hence in the inferred wind speed. This effect is dependent on the exact geometry and configuration of the ion chamber, which determine the degree to which ions produced from the stagnated gas component are trapped in the region of the electron beam (Ref. 33). In a

design with efficient trapping, an ion created from an incident neutral may see, if anything, a slight net positive potential at the electron beam and be analyzed as having a "head-wind" component of energy.

At the other extreme, in the UACS design there is an axial electric field component in the ion source which should prevent positive ion accumulation at low pressures. In this case, the unshielded electron beam imparts a net negative energy increment to incoming particles. In combination with the axial electric field, this negative well broadens the energy distribution of the incoming gas and restricts the capability to measure neutral temperature.

With higher pressures at lower altitudes, trapping of thermalized ions should resume and the net energy increment should change accordingly. From laboratory and flight data it appears that, without corrections, UACS wind measurements would be significantly affected at an altitude of 150 km with an energy offset equivalent to $\sim 200 \text{ m s}^{-1}$ in wind speed. Therefore, a source design that promotes efficient thermal ion trapping over the operating pressure range would minimize the potential well effect and simplify analysis of wind measurements. The shape of the retarding potential curve would be less altered, leading to more sensitive temperature measurements.

Finally, the intercomparison of data, done here to validate an experimental technique, also provides an example of the potential value of coordinated ground- and satellite-based measurements. It is likely that the combined data sets in Fig. 5 provide a better view of the low- and mid-latitudinal meridional wind profile near midnight than has been previously published. From this modest exercise, it is this author's impression that existing published wind data, together with unpublished data that must exist from ground stations and satellites AE-E and DE-B, could be used to synthesize a much more comprehensive picture of average wind patterns than now exists. This can certainly be done with new measurements by satellite-borne wind sensing instruments, such as UACS, in combination with the ever-increasing number of IS-radars and F-P observatories.

REFERENCES

1. P. B. Hays, T. L. Killeen, and B. C. Kennedy, "The Fabry-Perot Interferometer on Dynamics Explorer," Space Sci. Instrument., 5, 395-416 (1981).
2. R. A. Hoffman and E. R. Schmerling, "Dynamics Explorer Program: An Overview," Space Sci. Instrument., 5, 345-348 (1981).
3. T. L. Killeen, P. B. Hays, N. W. Spencer, and L. E. Wharton, "Neutral Winds in the Polar Thermosphere as Measured from Dynamics Explorer," Geophys. Res. Lett., 9, 957-960 (1982).
4. F. A. Marcos and J. M. Forbes, "Thermospheric Winds from the Satellite Electrostatic Triaxial Accelerometer System," J. Geophys. Res., 90, 6543-6552 (1985).
5. N. W. Spencer, Niemann, H. B., and Carignan, G. R., "The Neutral-Atmosphere Temperature Instrument," Radio Sci., 8, 287-296 (1973).
6. N. W. Spencer, R. F. Theis, L. E. Wharton, and G. R. Carignan, "Local Vertical Motions and Kinetic Temperature from AE-C as Evidence for Aurora-Induced Gravity Waves," Geophys. Res. Lett., 3, 313-316 (1976).
7. N. W. Spencer, G. R. Carignan, H. G. Mayr, H. B. Niemann, R. F. Theis, and L. E. Wharton, "The Midnight Temperature Maximum in the Earth's Equatorial Thermosphere," Geophys. Res. Lett., 6, 444-446 (1979).
8. J. R. Knutson, D. C. Kayser, and W. E. Potter, "Mass Spectrometric Measurement of Thermospheric Wind," J. Geophys. Res., 82, 5253-5256 (1977).
9. A. O. Nier, W. E. Potter, D. R. Hickman, and K. Mauersberger, "The Open-Source Neutral-Mass Spectrometer on Atmosphere Explorer-C, -D, and -E," Radio Sci., 8, 271-276 (1973).
10. A. O. Nier, W. E. Potter, D. C. Kayser, and R. G. Finstad, "The Measurement of Chemically Reactive Atmospheric Constituents by Mass Spectrometers Carried on High-Speed Spacecraft," Geophys. Res. Lett., 1, 197-200 (1974).
11. N. W. Spencer, L. E. Wharton, H. B. Niemann, A. E. Hedin, G. R. Carignan and J. C. Maurer, "The Dynamics Explorer Wind and Temperature Spectrometer," Space Sci. Instrument., 5, 417-428 (1981).
12. C. R. Philbrick, R. S. Narcisi, D. W. Baker, Trzcinski, E., and M. E. Gardner, "Satellite Measurements of Neutral Composition with a Velocity Mass Spectrometer," Space Res., 13, 321-325 (1973).
13. W. B. Hanson and R. A. Heelis, "Techniques for Measuring Bulk Gas Motions from Satellites," Space Sci. Instrument., 1, 493-524 (1975).

14. H. B. Niemann, J. R. Booth, J. E. Cooley, R. E. Hartle, W. T. Kasprzak, N. W. Spencer, S. H. Way, D. M. Hunten, and G. R. Carignan, "Pioneer Venus Orbiter Neutral Gas Mass Spectrometer Experiment," IEEE Trans. Geosci. Remote Sensing, GE-18, 60-65 (1980).
15. D. C. Kayser, W. T. Chater, C. K. Howey, and J. B. Pranke, "The Upper Atmosphere Composition Spectrometer," J. Spacecraft and Rockets, 23, 336-341 (1986).
16. E. G. Linder and K. G. Hernquist, "Space-Charge Effects in Electron Beams and Their Reduction by Positive Ion Trapping," J. Appl. Phys., 21, 1088-1097 (1950).
17. P. Amayenc, "Tidal Oscillations of the Meridional Neutral Wind at Mid-latitudes," Radio Sci., 9, 281-293 (1974).
18. R. G. Burnside, J. C. G. Walker, and M. P. Sulzer, "Kinematic Properties of the F-Region Ion Velocity Field Inferred from Incoherent Scatter Radar Measurements at Arecibo," J. Geophys. Res., 92, 3345-3355 (1987a).
19. G. Hernandez and R. G. Roble, "Direct Measurements of Nighttime Thermospheric Winds and Temperatures 1. Seasonal Variations During Geomagnetic Quiet Periods," J. Geophys. Res., 81, 2065-2074 (1976).
20. G. Hernandez and R. G. Roble, "The Geomagnetic Quiet Nighttime Thermospheric Wind Pattern Over Fritz Peak Observatory During Solar Cycle Minimum and Maximum," J. Geophys. Res., 89, 327-337 (1984).
21. D. P. Sipler, M. A. Biondi, and R. G. Roble, "F-Region Neutral Winds and Temperatures at Equatorial Latitudes: Measured and Predicted Behaviour During Geomagnetically Quiet Conditions," Planet. Space Sci., 31, 53-66 (1983).
22. D. P. Sipler and M. A. Biondi, "Equatorial F-Region Neutral Winds from Nightglow OI 630.0 nm Doppler Shifts," Geophys. Res. Lett., 5, 373-376 (1978).
23. D. P. Sipler, B. B. Luokkala, and M. A. Biondi, "Fabry-Perot Determinations of Midlatitude F-Region Neutral Winds and Temperatures from 1975 to 1979," Planet. Space Sci., 20, 1025-1032 (1982).
24. F. Jacka, A. R. O. Bower, and P. A. Wilksch, "Thermospheric Temperature and Winds Derived from OI λ 630 nm Night Airglow Line Profiles," J. Atmos. Terr. Phys., 41, 397-407 (1979).
25. G. Hernandez and R. G. Roble, "On Divergences of Thermospheric Meridional Winds at Mid-Latitudes," Geophys. Res. Lett., 6, 294-296 (1979).
26. G. Hernandez and R. G. Roble, "Direct Measurements of Nighttime Thermospheric Winds and Temperatures 3. Monthly Variations During Solar Minimum," J. Geophys. Res., 82, 5505-5511 (1977).

27. R. G. Burnside, C. A. Tepley, and V. B. Wickwar, "The O^+-O Collision Cross-Section: Can it be Inferred from Aeronomical Measurements?" J. Geophys. Res., 92, in press (1987b).
28. V. B. Wickwar, J. W. Meriwether, Jr., P.B. Hays, and A. F. Nagy, "The Meridional Thermospheric Neutral Wind Measured by Radar and Optical Techniques in the Auroral Region," J. Geophys. Res., 89, 10,987-10,998 (1984).
29. R. M. Harper, "Tidal Winds in the 100- to 200-km Region at Arecibo," J. Geophys. Res., 82, 3243-3250 (1977).
30. R. G. Burnside, R. A. Behnke, and J. C. G. Walker, "Meridional Neutral Winds in the Thermosphere at Arecibo: Simultaneous Incoherent Scatter and Airglow Observations," J. Geophys. Res., 88, 3181-3189 (1983).
31. L. E. Wharton, N. W. Spencer, and H. C. Brinton, "Correlations Between Neutral Meridional Winds and Ion Densities Observed on AE-E," J. Geophys. Res., 85, 4653-4657 (1980).
32. R. G. Burnside, F. A. Herrero, J. W. Meriwether, Jr., and J. C. G. Walker, "Optical Observations of Thermospheric Dynamics at Arecibo," J. Geophys. Res., 86, 5532-5540 (1981).
33. N. C. Barford, "Space Charge Neutralization by Ions in Linear Flow Electron Beams," J. Electron. Control, 3, 63-86 (1957).

LABORATORY OPERATIONS

The Aerospace Corporation functions as an "architect-engineer" for national security projects, specializing in advanced military space systems. Providing research support, the corporation's Laboratory Operations conducts experimental and theoretical investigations that focus on the application of scientific and technical advances to such systems. Vital to the success of these investigations is the technical staff's wide-ranging expertise and its ability to stay current with new developments. This expertise is enhanced by a research program aimed at dealing with the many problems associated with rapidly evolving space systems. Contributing their capabilities to the research effort are these individual laboratories:

Aerophysics Laboratory: Launch vehicle and reentry fluid mechanics, heat transfer and flight dynamics; chemical and electric propulsion, propellant chemistry, chemical dynamics, environmental chemistry, trace detection; spacecraft structural mechanics, contamination, thermal and structural control; high temperature thermomechanics, gas kinetics and radiation; cw and pulsed chemical and excimer laser development including chemical kinetics, spectroscopy, optical resonators, beam control, atmospheric propagation, laser effects and countermeasures.

Chemistry and Physics Laboratory: Atmospheric chemical reactions, atmospheric optics, light scattering, state-specific chemical reactions and radiative signatures of missile plumes, sensor out-of-field-of-view rejection, applied laser spectroscopy, laser chemistry, laser optoelectronics, solar cell physics, battery electrochemistry, space vacuum and radiation effects on materials, lubrication and surface phenomena, thermionic emission, photo-sensitive materials and detectors, atomic frequency standards, and environmental chemistry.

Computer Science Laboratory: Program verification, program translation, performance-sensitive system design, distributed architectures for spaceborne computers, fault-tolerant computer systems, artificial intelligence, micro-electronics applications, communication protocols, and computer security.

Electronics Research Laboratory: Microelectronics, solid-state device physics, compound semiconductors, radiation hardening; electro-optics, quantum electronics, solid-state lasers, optical propagation and communications; microwave semiconductor devices, microwave/millimeter wave measurements, diagnostics and radiometry, microwave/millimeter wave thermionic devices; atomic time and frequency standards; antennas, rf systems, electromagnetic propagation phenomena, space communication systems.

Materials Sciences Laboratory: Development of new materials: metals, alloys, ceramics, polymers and their composites, and new forms of carbon; non-destructive evaluation, component failure analysis and reliability; fracture mechanics and stress corrosion; analysis and evaluation of materials at cryogenic and elevated temperatures as well as in space and enemy-induced environments.

Space Sciences Laboratory: Magnetospheric, auroral and cosmic ray physics, wave-particle interactions, magnetospheric plasma waves; atmospheric and ionospheric physics, density and composition of the upper atmosphere, remote sensing using atmospheric radiation; solar physics, infrared astronomy, infrared signature analysis; effects of solar activity, magnetic storms and nuclear explosions on the earth's atmosphere, ionosphere and magnetosphere; effects of electromagnetic and particulate radiations on space systems; space instrumentation.

END

DATE

FILMED

DTIC

10-88